nanomaterials

MDPI

Article

On the Tensile Strength of Spark Plasma Sintered $AlMgB_{14}$ Ceramics

Pavel Nikitin, Ilya Zhukov *, Dmitrii Tkachev, Alexander Kozulin and Alexander Vorozhtsov

Laboratory of Metallurgy Nanotechnologies, National Research Tomsk State University, Lenin Avenue 36, 634050 Tomsk, Russia

* Correspondence: gofra930@gmail.com

Abstract: In this work, the structure, phase composition, hardness and tensile strength of the $AlMgB_{14}$-based material obtained by spark plasma sintering (SPS) were investigated. According to the XRD results, the spark plasma sintered material contains 94 wt% $AlMgB_{14}$ phase and 6 wt% spinel $MgAl_2O_4$. Analysis of the SEM images showed that the obtained $AlMgB_{14}$ sample has a dense structure; the relative density of the sample is 98.6%. The average microhardness of the spark plasma sintered (SPSed) sample is 29 ± 0.88 GPa. According to the results of the Brazilian test, the tensile strength of $AlMgB_{14}$ is 56 MPa. The fracture is characterized by a single straight tensile crack that divides the sample along the compression line into two halves. The type of fracture in the $AlMgB_{14}$ sample can be characterized as a cleavage fracture due to crack growth occurring in accordance with the transcrystalline fracture. The tensile strength of the obtained material is in good agreement with the tensile strength of boride and oxide ceramics studied in other works.

Keywords: $AlMgB_{14}$; tensile strength; Brazilian test; spark plasma sintering; CASTEP

Citation: Nikitin, P.; Zhukov, I.; Tkachev, D.; Kozulin, A.; Vorozhtsov, A. On the Tensile Strength of Spark Plasma Sintered $AlMgB_{14}$ Ceramics. *Nanomaterials* **2022**, *12*, 3805. https://doi.org/10.3390/nano12213805

Academic Editor: Shiqiang Hui

Received: 8 October 2022
Accepted: 27 October 2022
Published: 28 October 2022

1. Introduction

Superhard materials are characterized by a hardness of over 40 GPa [1]. Traditionally, diamond (HV = 80–100 GPa) and cubic boron nitride (HV = 60–80 GPa) are considered to be superhard materials [2]. It is known that solid materials have a high symmetry of the crystal lattice, the atoms of which have a strong interatomic bond. Thus, diamond has a strong sp^3 covalent bond in the tetrahedral lattice configuration, while cubic BN has the cF8 diamond structure and belongs to the class of superhard materials due to the strong covalent bond of BN [2]. However, obtaining boron nitride in a cubic configuration is extremely expensive due to the need for high temperature and pressure in the synthesis process [1]. In this regard, the search for hard materials with excellent mechanical properties is an urgent scientific problem. To date, the attention of researchers is attracted by boron carbide (B_4C), titanium diboride (TiB_2) [3–7], cubic silicon carbide (β-SiC) [8], titanium carbide (TiC) [9,10], etc. Despite the fact that these materials cannot formally be classified as superhard, in the form of thin-film coatings, they demonstrate hardness values above 40 GPa [11].

It is important to note that all of the above materials have a simple symmetrical structure that satisfies the traditional paradigm of superhard materials [2,12,13]. However, since 2000, $AlMgB_{14}$-based materials, which have a complex low-symmetric orthorhombic structure and, at the same time, high properties, have been actively studied. Aluminum magnesium boride ($AlMgB_{14}$) has many excellent physical properties, such as high hardness (up to 32 GPa), relatively low density (2.59 g/cm^3), oxidation resistance, excellent wear resistance and a very low coefficient of friction (up to 0.02) [2,14–16]. In combination with titanium diboride, materials based on $AlMgB_{14}$ demonstrate hardness reaching 46 GPa [2], which classifies $AlMgB_{14}$–TiB_2 composite materials as superhard. As of yet, the main efforts of scientists have been directed at studying the influence of production methods (one-stage or two-stage sintering) and the composition of the initial mixture (ratio of initial elements,

pre-reacted powders or mechanical mixture) on the structure, phase formation processes and properties of $AlMgB_{14}$-based materials [13–26]. Today, it is traditionally considered that the best sintering methods for obtaining $AlMgB_{14}$ are spark plasma sintering and hot pressing of $AlMgB_{14}$ powder mixtures [2,14–17,21–23]. At the same time, the properties of the obtained materials are mainly influenced by the purity of the material (the presence of $MgAl_2O_4$ spinel in the samples leads to a significant decrease in the properties of $AlMgB_{14}$ [27]). Nevertheless, despite the comprehensive number of publications devoted to the study of hardness, density, oxidation resistance, friction coefficients, coefficients of thermal expansion (CTE), and other properties of $AlMgB_{14}$-based materials [2,14–19,28], there are no publications on their strength characteristics, in particular, on the tensile strength/flexural strength/compressive strength. At the same time, the tensile strength plays an important role in the analysis of the failure mechanism of structural ceramics and in the design of various structural ceramic parts; therefore, obtaining data on the strength characteristics of $AlMgB_{14}$ is an important research task.

Tensile strength can be determined mainly by the direct tensile test and the Brazilian test. Conducting tensile experiments on ceramics is too difficult due to their low fracture strain. In turn, the Brazilian test, an indirect tensile method, is a popular choice for testing ceramic materials [29,30] due to the ease of material preparation and testing. Thus, the purpose of this work is to study the tensile strength using the Brazilian test, as well as the structure and the phase composition of $AlMgB_{14}$ ceramics obtained by spark plasma sintering.

2. Materials and Methods

2.1. Process for Obtaining $AlMgB_{14}$-Based Ceramics

$AlMgB_{14}$-based ceramics were obtained by spark plasma sintering (DR. SINTER model SPS-625 Spark Plasma Sintering System, SPS SYNTEX INC. Ltd., Tokyo, Japan) of the $Al_{12}Mg_{17}$-B powder mixture at a pressure of 70 MPa and a temperature of 1400 °C. The working chamber was evacuated to a vacuum level of 6 Pa. Mechanical pressure was applied to the graphite die in the first minute of the sintering process and kept constant throughout the process. The sample was heated from room temperature to 1400 °C at a heating rate of 50 °C min^{-1}. The diameter and thickness of the obtained samples were ~12.5 mm and 3 mm, respectively. The sintered sample was polished for further research. The characteristics of the raw powders are given in Table 1. To obtain a mixture of $Al_{12}Mg_{17}$-B, the powders of $Al_{12}Mg_{17}$ and amorphous black boron were mixed in an atomic ratio of 2:14 and mechanically activated (MA) in a planetary mill (Activator 4M, Engineering Plant "Activator", Ltd., Dorogino, Russia) for 3 h in an argon atmosphere with a rotational frequency of 14 Hz. The mass ratio of grinding bodies to the powder mixture was 3:1. The average size of the resulting $Al_{12}Mg_{17}$-B powder mixture was 400 nm.

Table 1. Characteristics of the raw powders.

Powder	Average Particle Size	Purity, %
$Al_{12}Mg_{17}$	15 μm	≥99.2
Amorphous B	600 nm	≥98.7
MA-$Al_{12}Mg_{17}$-B	400 nm	≥98.8

2.2. Brazilian Test

Tests at 24 °C and a loading rate of 0.75 mm/min were performed on an Instron 3369 double column testing machine. The specimens were placed in the testing machine between flat plates such that the loading force was applied along the center line of the specimen base. The ASTM D3967 (Brazilian test for brittle materials) recommended formula for calculating the tensile strength of a test material is given below:

$$\sigma_t = 2P/\pi LD = 0.636P/LD$$

where σ_t is the splitting stress (MPa), which is the value of the indirect tensile strength; *P*—the maximum applied force (N), is selected from the maximum value of the experimental curve "force–displacement"; *L* is the sample thickness (mm); *D* is the sample diameter (mm).

2.3. Characterization

X-ray diffraction analysis of the obtained sample was performed using a Shimadzu 6000 diffractometer with CuKα radiation and using the PDF-4 (Powder Diffraction File) database. The phase composition was refined using the Rietveld method. For this work, the CASTEP program code [31] was used to calculate the energies of the referenced and refined crystal lattices within the framework of the density functional theory (DFT). The exchange–correlation potential was treated within the generalized gradient approximation (GGA) using the Perdew–Burke–Ernzerhof (PBE-GGA) scheme [32]. A plane-wave cutoff energy of 500 eV was used. The microstructure of the obtained sample was determined using a QUANTA 3D microscope with energy dispersive spectroscopy (EDX). The density of the sintered sample was calculated using the Archimedes method. The Vickers hardness (HV) was determined using a Metolab-502 microhardness tester at a load of 1 kg (9.8 N). The loading time was 10 s. Ten indentations were made from different places of the sample.

3. Results

3.1. Microstructure and Phase Composition of the Obtained $AlMgB_{14}$ Ceramics

The results of the XRD analysis of the spark plasma sintered $AlMgB_{14}$ sample are shown in Figure 1. Analysis of the contributions to the weight intensity of individual phases (Table 2, Figure 1) showed that in the obtained samples the main phases are $AlMgB_{14}$ and $MgAl_2O_4$. The experimental XRD pattern (Figure 1, violet symbols) of the obtained composite is closely approximated by the calculated integral intensity (Figure 1, black line); the difference between them is insignificant (Figure 1, orange line).

Table 2. Structural parameters of lattices.

Phase	State	a, Å	b, Å	c, Å	α = β = γ	V, Å^3	E, eV
$AlMgB_{14}$	Reference	5.850	8.111	10.310	90	489.202	−8451.883
	Refined	5.851	8.112	10.311	90	489.394	−8451.884
$MgAl_2O_4$	Reference	8.083	8.083	8.083	90	528.101	−22767.860
	Refined	8.045	8.045	8.045	90	520.688	−22767.475

Using the Rietveld method, the quantitative content of the phases was determined. It was found that the weight content of the $AlMgB_{14}$ phase is dominant and amounts to 94 wt%, while the content of spinel $MgAl_2O_4$ in the obtained samples is no higher than 6 wt%. Structural parameters (a, b, c, α, β, γ) and the free energy (E) of the crystal lattices of $AlMgB_{14}$ and $MgAl_2O_4$ in both the reference and the refined states are given in Table 2. As can be seen from Table 2, the structural parameters of the $AlMgB_{14}$ lattice do not change. At the same time, the lattice volume V of the $MgAl_2O_4$ spinel changes significantly from 528.101 (reference state) to 520.688 (refined state) Å^3. The lattice energy of $MgAl_2O_4$ in the refined state is higher than in the reference state, which indicates a lower lattice stability.

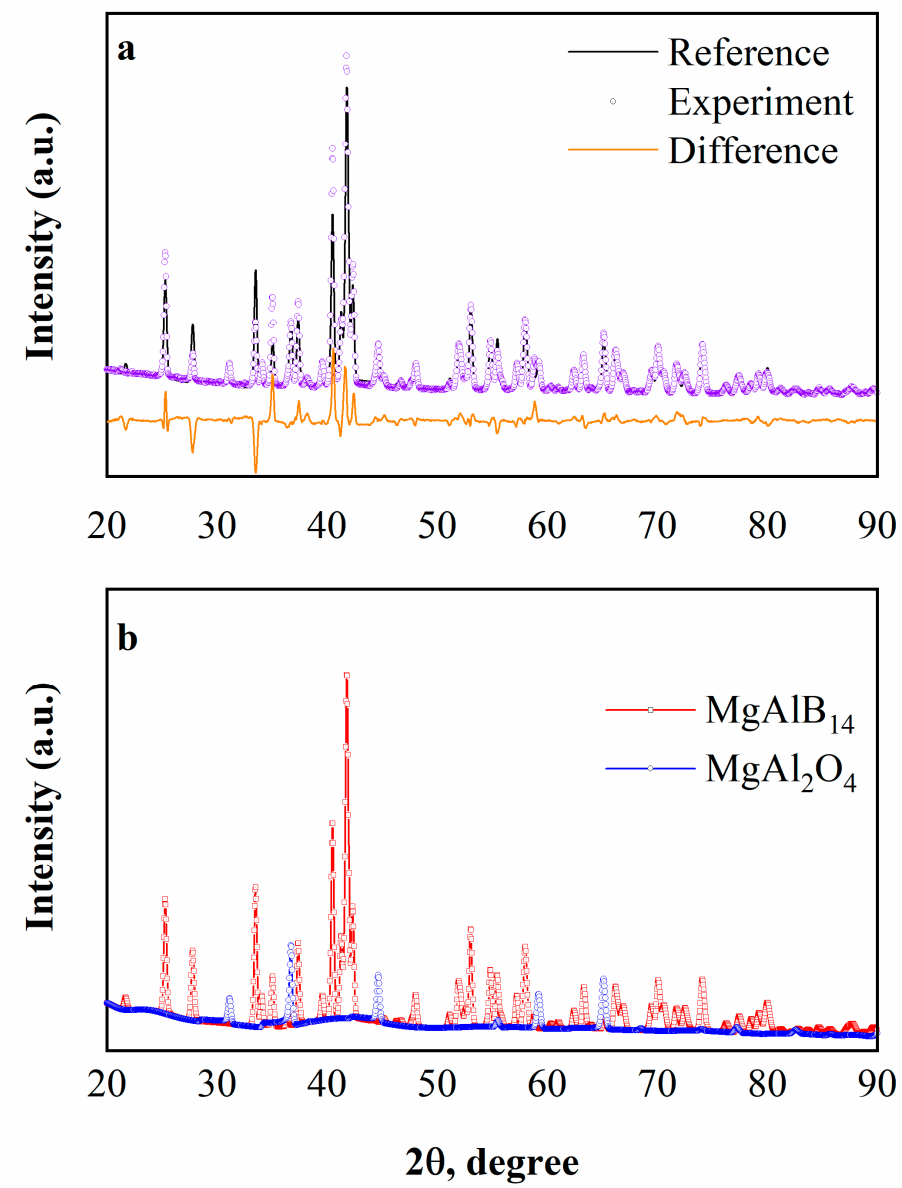

Figure 1. XRD patterns of the spark plasma sintered $AlMgB_{14}$ samples: (**a**) 1—experimental XRD pattern (violet symbols), 2—integral intensity found using the Rietveld method (black line), 3—difference between experimental and integral intensities (orange line); (**b**) theoretical XRD patterns of the $AlMgB_{14}$ and $MgAl_2O_4$ phases, found using the Rietveld method.

The microstructure of the sintered sample is shown in Figure 2. As can be seen from Figure 2, spark plasma sintering of the $Al_{12}Mg_{17}$-B powder mixture leads to the formation of a dense homogeneous structure with inclusions of the oxide phase. According to the EDX results of the orange area in Figure 2, O, Al and Mg elements were found in the light areas ($MgAl_2O_4$ phase). In the dark areas, B, Al and Mg elements were found in the ratio corresponding to the $AlMgB_{14}$ phase. EDX spectra are given in the Supplementary Materials. In the structure of the obtained sample, single pores with an average size of 3 μm were observed. The average grain size in the sintered samples is 3–5 μm. Based on the calculations using the Archimedes method, the relative density of the $AlMgB_{14}$-based sample is 98.6% (if we take into account the 6% content of $MgAl_2O_4$ spinel, the theoretical density of the sample is 2.63 g/cm^3).

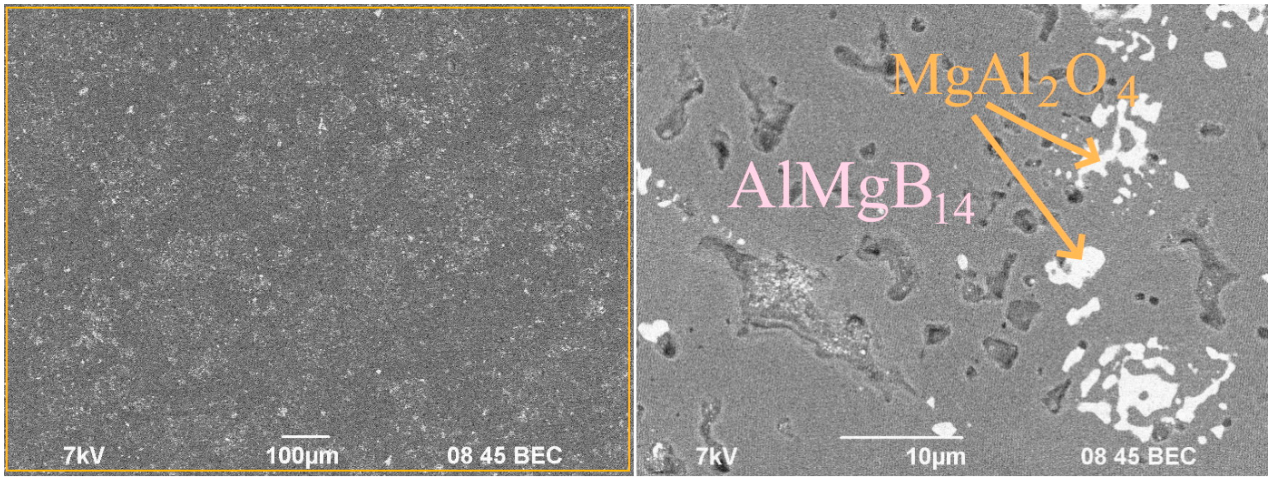

Figure 2. SEM images of the surface of the $AlMgB_{14}$ sample.

3.2. Mechanical Properties of the Sintered Sample

The results of the hardness measurements of the obtained materials based on $AlMgB_{14}$ are shown in Table 3. The average hardness of the obtained sample is 29 ± 0.88 GPa. The reported values of microhardness of the $AlMgB_{14}$-based materials are 27.87 ± 0.97 [14], 26.7 ± 2.2 [15] and 26.1 [16] GPa, respectively. Thus, the value obtained in this work is in good agreement with the reported data [2,14–17,21,22].

Table 3. The results of measuring the hardness of the obtained sample.

Measurement Number/HV										HV_{av}, GPa
1	2	3	4	5	6	7	8	9	10	29.00 ± 0.88
2743.9	2795.6	2858.0	3050.8	2903.4	2805.4	2795.6	2931.3	3073.3	3073.3	

Figure 3a shows the dependence of the change in the loading force applied to the $AlMgB_{14}$ sample on the displacement during the experiment for the Brazilian test at a temperature of 24 °C and a loading rate of 0.75 mm/min (10^{-3} s^{-1}). According to the obtained results, the tensile strength of $AlMgB_{14}$ is 56 MPa.

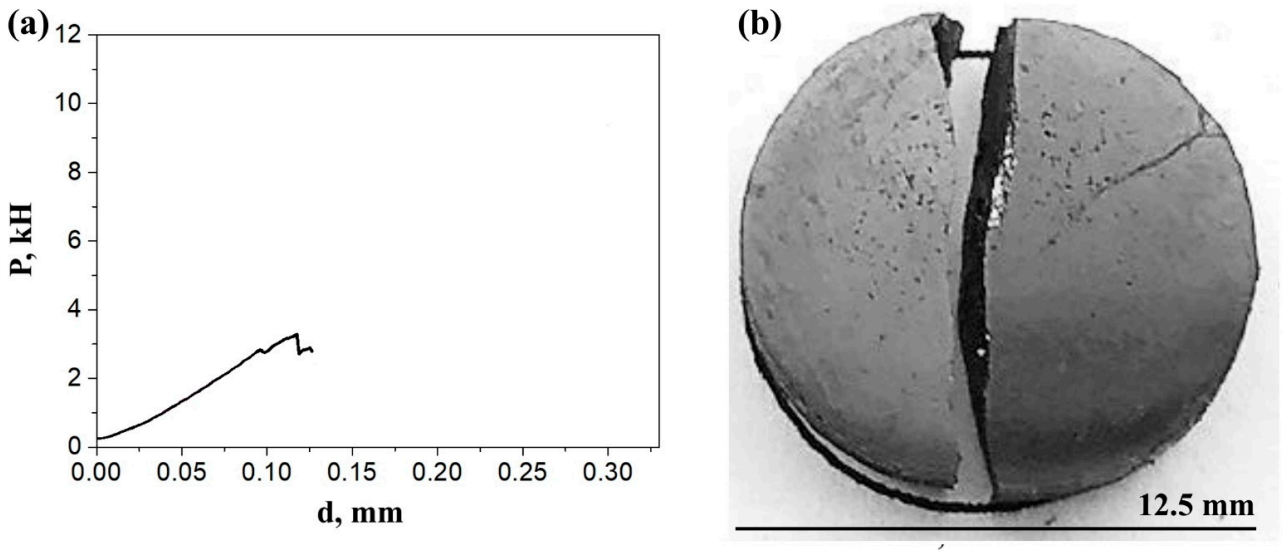

Figure 3. *Cont.*

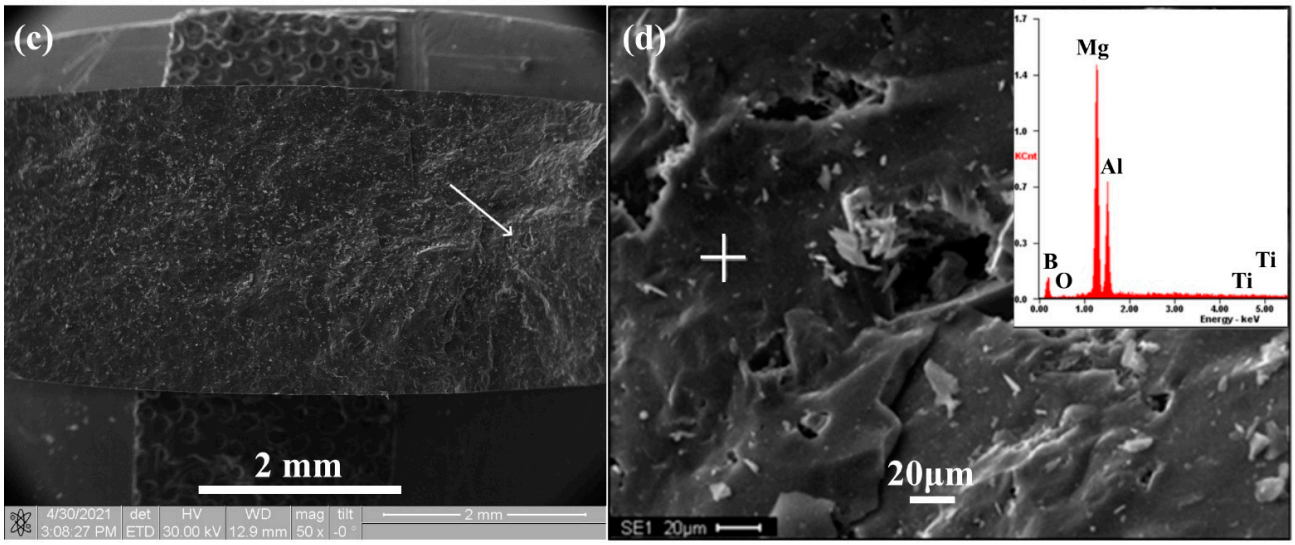

Figure 3. (**a**) The dependence of the change in the loading force on the $AlMgB_{14}$ sample, obtained from the displacement during the experiment for the Brazilian test at a temperature of 24 °C and a loading speed of 0.75 mm/min; (**b**) the appearance of the $AlMgB_{14}$ sample, fractured after the Brazilian test; (**c**) macro- and (**d**) micro-images of the fracture surface of the $AlMgB_{14}$ sample.

4. Discussion

The appearance of the $AlMgB_{14}$ sample, fractured after the Brazilian test, is shown in Figure 3b. Analyzing the image of a fractured $AlMgB_{14}$ sample after the Brazilian test, we observe that the fracture is characterized by a single straight tensile crack that splits the specimen along the compression line into two halves. This failure is considered typical for loading conditions in the Brazilian test in terms of analytical strength theory assumptions [33–35]. At the same time, in [36,37], the fracture of ceramic materials after the Brazilian test was accompanied by a ternary fracture and multiple branching cracks. Such a fracture pattern can be explained by the inhomogeneous phase composition, which leads to dispersion strengthening due to inclusions with mechanical characteristics that differ from the base material. Thus, the $AlMgB_{14}$-based material obtained in this study has a homogeneous phase composition, and therefore the fracture is characterized by a single straight crack.

The SEM image of the fracture surface of the $AlMgB_{14}$ sample and the integrated elemental analysis of a typical microsection on the fracture surface are shown in Figure 3c,d. The crack initiation region is marked with a white arrow in Figure 3c. The initiation of a crack in the sample occurred not far from the central region of the sample, closer to the loading point. Most of the fracture surface, except for the crack initiation area, is relatively smooth without sharp drops and relief changes. Obviously, when under tension, the crack grew without resistance in local centers, which indicates the homogeneity of the composition and internal structure. The type of fracture can be characterized as a cleavage fracture due to crack growth occurring in accordance with the transcrystalline scenario. Multiple small fragments of the same elemental composition (Figure 3d) as the integral composition of the material were found on the fracture surface, with a predominance of Al, Mg and B chemical elements. The presence of other elements across the entire fracture surface is determined at the level of error (Table 4). A small number of micropores were also found, distributed evenly across the entire destruction surface with sizes not exceeding 20 µm.

Table 4. Results of the elemental analysis of a typical microsection on the fracture surface.

Element	B	Al	Mg	O	Ti
Wt%	87.6	4.10	8.00	0.25	0.05

The tensile strength of the obtained $AlMgB_{14}$-based material is in good agreement with the tensile strength of the various ceramics studied in other works (Table 5). Apparently, the lower tensile strength of $AlMgB_{14}$ compared to other ceramics can be associated with its complex low-symmetry orthorhombic crystal lattice and the presence of pores and microdefects in its structure. At the same time, as can be seen from Table 5, the composite material based on Al_2O_3–ZrO_2 eutectic has the highest tensile strength. Due to the presence of the second phase in the structure of the material and due to phase transformations in the ZrO_2 during destruction, the propagating cracks can branch and stop. In [2], a significant increase in the hardness of $AlMgB_{14}$-based materials was reported due to the introduction of additives. With the addition of silicon, the hardness of $AlMgB_{14}$ increased to 35 GPa; with the addition of titanium diboride, it increased to 46 GPa. In [38], the authors reported that $AlMgB_{14}$ and TiB_2 have an exceptionally strong bond due to very close values of their surface energies. In $AlMgB_{14}$–TiB_2 composite materials, $AlMgB_{14}$ provides both good wetting and internal strength of the composite. In combination, these two borides can provide a high degree of mutual enhancement [38]. Based on the above, in the future, it will be of great interest to study the tensile strength of $AlMgB_{14}$–TiB_2 composite materials.

Table 5. Comparison of the tensile strength of $AlMgB_{14}$ with other ceramics.

Material	σ_t, MPa	Reference
$AlMgB_{14}$	56.0	This work
Al_2O_3–$ZrO_2(Y_2O_3)$ eutectics	80.0	[39]
HfB_2	53.8	[40]
TiB_2	60.2	[40]
ZrB_2	53.3	[40]

5. Conclusions

In this work, the $AlMgB_{14}$-based ceramic material was obtained by spark plasma sintering. The mechanical properties, structure and phase composition were studied. The $AlMgB_{14}$ phase content in the obtained sample was 94 wt% with a spinel $MgAl_2O_4$ content no higher than 6 wt%. According to the results of density and hardness measurements, the relative density of the sintered $AlMgB_{14}$-based material was 98.6% with an average microhardness of 29 GPa. According to the results of the Brazilian test, the tensile strength of $AlMgB_{14}$ was 56 MPa. The fracture is characterized by a single straight tensile crack that divides the sample along the compression line into two halves. The type of fracture of the $AlMgB_{14}$ sample can be characterized as a cleavage fracture due to its crack growth appearing in accordance with the transcrystalline fracture. The tensile strength of the obtained material is in good agreement with the tensile strength of boride and oxide ceramics studied in other works.

Supplementary Materials: The following supporting information can be downloaded at: https://www.mdpi.com/article/10.3390/nano12213805/s1. EDX spectra are given in the Supplementary Materials.

Author Contributions: Conceptualization, P.N.; methodology, P.N., I.Z. and A.K.; investigation, P.N., I.Z., A.K. and D.T.; resources, I.Z. and A.V.; writing—original draft preparation, P.N.; writing—review and editing, P.N. and I.Z.; visualization, P.N.; funding acquisition, I.Z. All authors have read and agreed to the published version of the manuscript.

Funding: This work was carried out with financial support from the Ministry of Education and Science of the Russian Federation (State assignment No. FSWM-2020-0028).

Data Availability Statement: The data presented in this study are available in the article.

Acknowledgments: The SEM research was carried out with the equipment of Tomsk Regional Core Shared Research Facilities Center of National Research Tomsk State University (Grant of the Ministry of Science and Higher Education of the Russian Federation no. 075-15-2021-693 (no. 13.RFC.21.0012)).

Conflicts of Interest: The authors declare no conflict of interest.

References

1. Wentorf, R.H.; DeVries, R.C.; Bundy, F.P. Sintered Superhard Materials. *Science* **1980**, *208*, 873–880. [CrossRef] [PubMed]
2. Cook, B.A.; Harringa, J.L.; Lewis, T.L.; Russel, A.M. A new class of ultra-hard materials based on $AlMgB_{14}$. *Scr. Mater.* **2000**, *42*, 597–602. [CrossRef]
3. Nguyen, T.P.; Mahaseni, Z.H.; Germi, M.D.; Delbari, S.A.; Van Le, Q.; Ahmadi, Z.; Namini, A.S. Densification behavior and microstructure development in TiB_2 ceramics doped with h-BN. *Ceram. Int.* **2020**, *46*, 18970–18975. [CrossRef]
4. Matveev, A.E.; Zhukov, I.A.; Ziatdinov, M.H.; Zhukov, A.S. Planetary Milling and Self-Propagating High-Temperature Synthesis of Al-TiB_2 Composites. *Material* **2020**, *13*, 1050. [CrossRef] [PubMed]
5. Matveev, A.; Promakhov, V.; Nikitin, P.; Babaev, A.; Vorozhtsov, A. Effect of Mechanical Activation of Al-Ti-B Powder Mixture on Phase Composition and Structure of Al-TiB_2 Composite Materials Obtained by Self-Propagating High-Temperature Synthesis (SHS). *Materials* **2022**, *15*, 2668. [CrossRef]
6. Promakhov, V.; Matveev, A.; Schulz, N.; Dronov, P.; Zhukov, A.; Vorozhtsov, A. Structure, Properties and Phase Composition of Composite Materials Based on the System NiTi-TiB_2. *Materials* **2022**, *15*, 5327. [CrossRef]
7. Evseev, N.S.; Matveev, A.E.; Nikitin, P.Y.; Abzaev, Y.A.; Zhukov, I.A. A theoretical and experimental investigation on the SHS synthesis of (HfTiCN)-TiB_2 high-entropy composite. *Ceram. Int.* **2022**, *48*, 16010–16014. [CrossRef]
8. Pant, H.K.; Debnath, D.; Chakraborty, S.; Wani, M.F.; Das, P.K. Mechanical and tribological properties of spark plasma sintered SiC–TiB_2 and SiC–TiB_2–TaC composites: Effects of sintering temperatures (2000 °C and 2100 °C). *J. Tribol.* **2018**, *140*, 011608. [CrossRef]
9. Vallauri, D.; Adrián, I.A.; Chrysanthou, A. TiC–TiB_2 composites: A review of phase relationships, processing and properties. *J. Eur. Ceram. Soc.* **2008**, *28*, 1697–1713. [CrossRef]
10. Matveev, A.E.; Nikitin, P.Y.; Zhukov, I.A.; Zhukov, A.S. The use of plastic waste as carbon raw materials to obtain TiC-based powders. *Ceram. Int.* **2021**, *47*, 21140–21146. [CrossRef]
11. Liao, F.; Girshick, S.L.; Mook, W.M.; Gerberich, W.W.; Zachariah, M.R. Superhard nanocrystalline silicon carbide films. *Appl. Phys. Lett.* **2005**, *86*, 171913. [CrossRef]
12. Teter, D.M. Computational alchemy: The search for new superhard materials. *MRS Bull.* **1998**, *23*, 22–27. [CrossRef]
13. Lowther, J.E. Possible ultra-hard materials based upon boron icosahedra. *Phys. B Condens. Matter* **2002**, *322*, 173–178. [CrossRef]
14. Kevorkijan, S.D.; Škapin, M.; Jelen, K.; Krnel, A. Meden, Cost-effective synthesis of $AlMgB_{14}$–xTiB_2. *J. Eur. Ceram. Soc.* **2007**, *27*, 493–497. [CrossRef]
15. Xie, Z.; DeLucca, V.; Haber, R.A.; Restrepo, D.T.; Todd, J.; Blair, R.G.; Orlovskaya, N. Aluminum magnesium boride: Synthesis, sintering and microstructure. *Adv. Appl. Ceram.* **2017**, *116*, 341–347. [CrossRef]
16. Roberts, D.J.; Zhao, J.; Munir, Z.A. Mechanism of reactive sintering of $MgAlB_{14}$ by pulse electric current. *Int. J. Refract. Hard Met.* **2009**, *27*, 556–563. [CrossRef]
17. Nikitin, P.Y.; Zhukov, I.A.; Matveev, A.E.; Sokolov, S.D.; Boldin, M.S.; Vorozhtsov, A.B. $AlMgB_{14}$–TiB_2 composite materials obtained by self-propagating high-temperature synthesis and spark plasma sintering. *Ceram. Int.* **2020**, *46*, 22733–22737. [CrossRef]
18. Nikitin, P.Y.; Matveev, A.E.; Zhukov, I.A. Energy-effective $AlMgB_{14}$ production by self-propagating high-temperature synthesis (SHS) using the chemical furnace as a source of heat energy. *Ceram. Int.* **2021**, *47*, 21698–21704. [CrossRef]
19. Chen, J.; Cheng, J.; Li, F.; Zhu, S.; Li, W.; Yang, J.; Liu, W. Tribological study on a novel wear-resistant $AlMgB_{14}$-Si composite. *Ceram. Int.* **2017**, *43*, 12362–12371. [CrossRef]
20. Zhukov, I.A.; Ziatdinov, M.K.; Dubkova, Y.A.; Nikitin, P.Y. Synthesis of $AlMgB_{14}$: Influence of Mechanical Activation of Al–Mg–B Powder Mixture on Phase Composition of Sintered Materials. *Russ. Phys. J.* **2018**, *61*, 1466–1471. [CrossRef]
21. Zhukov, I.A.; Nikitin, P.Y.; Vorozhtsov, A.B.; Perevislov, S.N.; Sokolov, S.D.; Ziatdinov, M.H. The use of intermetallic AlxMgy powder to obtain $AlMgB_{14}$-based materials. *Mater. Today Commun.* **2020**, *22*, 100848. [CrossRef]
22. Nikitin, P.Y.; Zhukov, I.A.; Vorozhtsov, A.B. Decomposition mechanism of $AlMgB_{14}$ during the spark plasma sintering. *J. Mater. Res. Technol.* **2020**, *11*, 687–692. [CrossRef]
23. Nikitin, P.; Zhukov, I.; Matveev, A.; Sokolov, S.; Grigoriev, M.; Vorozhtsov, A. On the Structure and Properties of $AlMgB_{14}$-TiB_2 Composites Obtained from SHS Powders by Spark Plasma Sintering. *Materials* **2021**, *14*, 5521. [CrossRef]
24. Nikitin, P.; Zhukov, I.; Matveev, A.; Sokolov, S.; Sachkov, V.; Vorozhtsov, A. Phase Composition, Structure and Properties of the Spark Plasma Sintered Ceramics Obtained from the $Al_{12}Mg_{17}$-B-Si Powder Mixtures. *Nanomaterials* **2022**, *12*, 1895. [CrossRef] [PubMed]
25. Cheng, J.; Ma, J.; Li, F.; Qiao, Z.; Yang, J.; Liu, W. Dry-sliding tribological properties of Cu/$AlMgB_{14}$ composites. *Tribol. Lett.* **2014**, *55*, 35–44. [CrossRef]

26. Sun, Y.Y.; Zhang, P.X.; Liu, G.Q.; Xiong, X.M.; Yang, F.; Jiao, G.F.; Yan, G. Effect of two-step heat treatment on the phase formation of $MgAlB_{14}$. *Mater. Lett.* **2011**, *65*, 2158–2160. [CrossRef]
27. Lewis, T.L.; Cook, B.A.; Harringa, J.L.; Russell, A.M. Al_2MgO_4, Fe_3O_4, and FeB impurities in $AlMgB_{14}$. *Mater. Sci. Eng. A* **2003**, *351*, 117–122. [CrossRef]
28. Russell, A.M.; Cook, B.A.; Harringa, J.L.; Lewis, T.L. Coefficient of thermal expansion of $AlMgB_{14}$. *Scr. Mater.* **2002**, *46*, 629–633. [CrossRef]
29. Aliha, M.R.M.; Ayatollahi, M.R. Analysis of fracture initiation angle in some cracked ceramics using the generalized maximum tangential stress criterion. *Int. J. Solids Struct.* **2012**, *49*, 1877–1883. [CrossRef]
30. Brückner-Foit, A.; Fett, T.; Munz, D.; Schirmer, K. Discrimination of multiaxiality criteria with the Brazilian disc test. *J. Eur. Ceram. Soc.* **1997**, *17*, 689–696. [CrossRef]
31. Clark, S.J.; Segall, M.D.; Pickard, C.J.; Hasnip, P.J.; Probert, M.I.; Refson, K.; Payne, M.C. First principles methods using CASTEP. *Z. Für Krist.-Cryst. Mater.* **2005**, *220*, 567–570. [CrossRef]
32. Perdew, J.P.; Burke, K.; Ernzerhof, M. Generalized gradient approximation made simple. *Phys. Rev. Lett.* **1996**, *77*, 3865. [CrossRef] [PubMed]
33. Carmona, S.; Aguado, A. New model for the indirect determination of the tensile stress–strain curve of concrete by means of the Brazilian test. *Mater. Struct.* **2012**, *45*, 1473–1485. [CrossRef]
34. Colback, P.S.B. An analysis of brittle fracture initiation and propagation in the Brazilian test. In Proceedings of the 1st ISRM Congress, Lisbon, Portugal, 25 September–1 October 1966.
35. García, V.J.; Márquez, C.O.; Zúñiga-Suárez, A.R.; Zuñiga-Torres, B.C.; Villalta-Granda, L.J. Brazilian test of concrete specimens subjected to different loading geometries: Review and new insights. *Int. J. Concr. Struct. Mater.* **2017**, *11*, 343–363. [CrossRef]
36. Serati, M.; Masoumi, H.; Williams, D.J.; Alehossein, H. Modified Brazilian test for indirect measurement of tensile strength of brittle materials. In Proceedings of the 51st US Rock Mechanics/Geomechanics Symposium, San Francisco, CA, USA, 25–28 June 2017.
37. Dai, Y.; Li, Y.; Xu, X.; Zhu, Q.; Yan, W.; Jin, S.; Harmuth, H. Fracture behaviour of magnesia refractory materials in tension with the Brazilian test. *J. Eur. Ceram. Soc.* **2019**, *39*, 5433–5441. [CrossRef]
38. Cook, B.A.; Russell, A.M.; Peters, J.; Harringa, J.L. Estimation of surface energy and bonding between $AlMgB_{14}$ and TiB_2. *J. Phys. Chem. Solids* **2010**, *71*, 824–826. [CrossRef]
39. Pastor, J.Y.; Poza, P.; Llorca, J.; Pena, J.I.; Merino, R.I.; Orera, V.M. Mechanical properties of directionally solidified Al_2O_3–ZrO_2 (Y_2O_3) eutectics. *Mater. Sci. Eng. A* **2001**, *308*, 241–249. [CrossRef]
40. Zhang, X.; Luo, X.; Li, J.; Hu, P.; Han, J. The ideal strength of transition metal diborides TMB_2 (TM = Ti, Zr, Hf): Plastic anisotropy and the role of prismatic slip. *Scr. Mater.* **2010**, *62*, 625–628. [CrossRef]